# Turbulence in rotating Bose-Einstein condensates

Julian Amette Estrada [1,*] Marc E. Brachet [2,†] and Pablo D. Mininni [1,‡]

[1]*Departamento de Física, Facultad de Ciencias Exactas y Naturales, Universidad de Buenos Aires and IFIBA, CONICET, Ciudad Universitaria, 1428 Buenos Aires, Argentina*

[2]*Laboratoire de Physique Statistique, École Normale Supérieure, PSL Research University; UPMC Université Paris 06, Sorbonne Universités; Université Paris Diderot, Sorbonne Paris-Cité; and CNRS, 24 Rue Lhomond, 75005 Paris, France*

(Received 27 January 2022; accepted 1 June 2022; published 22 June 2022)

Since the idea of quantum turbulence was first proposed by Feynman and later realized in experiments of superfluid helium and Bose-Einstein condensates, much emphasis has been put on finding signatures that distinguish quantum turbulence from its classical counterpart. Here we show that quantum turbulence in rotating condensates is fundamentally different from the classical case. While rotating quantum turbulence develops a negative temperature state with self-organization of the kinetic energy in quantized vortices, it also displays an anisotropic dissipation mechanism and a different, non-Kolmogorovian, scaling of the energy at small scales. This scaling is compatible with Vinen turbulence and also has been found in recent simulations of condensates with multicharged vortices. An elementary explanation for the scaling is presented in terms of disorder in the vortices positions.

DOI: 10.1103/PhysRevA.105.063321

## I. INTRODUCTION

Quantum turbulence corresponds to the chaotic and out-of-equilibrium dynamics of quantized vortices observed in Bose-Einstein condensates (BECs) and in superfluid helium. Turbulence in both physical systems has been studied in laboratory experiments [1–5] as well as theoretically and numerically [6–11].

Under many circumstances, quantum turbulence is very similar to its classical counterpart, to the point that identifying their distinguishing features became a major research topic. Many times both display Kolmogorov scaling $E(k) \sim k^{-5/3}$ of the kinetic energy, even though the mechanism behind this scaling in the quantum regime is believed to be vortex reconnection at large scales and a cascade of Kelvin waves at small scales [7], the latter mechanism being unavailable in classical turbulence. However, some experiments [12–14] show another regime known as Vinen turbulence (or the "ultraquantum" regime), with $E(k) \sim k^{-1}$ scaling and with no classical counterpart. In this regime a thermal counterflow is believed to play an important role in the dynamics. This scaling was also found in numerical simulations with counterflow [15,16], but more intriguingly also more recently in simulations of BECs with an initial array of ordered vortices and no apparent counterflow [17,18] as well as in simulations of homogeneous superfluid turbulence [19].

Rotating BECs display many interesting regimes that connect the flow dynamics and steady states with condensed matter physics [20], including ordered vortex lattices [21,22] and global modes and waves which have no classical counterparts [23–25]. In spite of this, or perhaps because of its complexity, turbulence in rotating BECs has not been thoroughly studied so far. A recent numerical study considered rotating turbulence in unitary Fermi gases [26], finding differences in the dissipation mechanisms between fermionic and bosonic superfluids. However, a detailed comparison against classical fluids is still lacking. In classical turbulence, rotation generates a significant change in the system dynamics. The flow becomes quasi-two-dimensional, a steeper-than-Kolmogorov spectrum $E(k) \sim k^{-2}$ develops at small scales [27–30] in which inertial waves play a central role, and at large scales the flow self-organizes in columns with an inverse cascade of energy [31,32].

For a detailed discussion on the theory of classical rotating turbulence, see Ref. [33]. In the limit of very rapidly rotating incompressible flows and in infinite domains, the flow becomes strongly anisotropic and the energy is mostly contained in inertial waves. This allows for wave-turbulence descriptions of the system [33,34]. In this rapidly rotating limit, the $\sim k_\perp^{-2}$ energy spectrum results only for wave vectors in Fourier space close to the plane perpendicular to the axis of rotation, and the energy is transferred solely from large to small scales. The inverse energy cascade [i.e., the self-similar preferential transfer of energy towards large-scale modes and in particular towards two-dimensional (2D) modes] vanishes in the limit of angular velocity $\Omega \to \infty$ and of the domain height $H \to \infty$ [33]. For moderate rotation rates $\Omega$ and for finite domain heights, the inverse energy cascade can be recovered (see [31,32] and a rigorous wave turbulence study in [35]). It is important to note that the latter is the regime of interest when comparing with rotating BECs, as condensates in experiments are constrained by an external potential and as for very large values of $\Omega$ a quantum phase transition to a different many-body state that does not have a BEC is expected [20].

*julianamette@df.uba.ar
†brachet@physique.ens.fr
‡mininni@df.uba.ar

 

In this work we study turbulence in rotating BECs in the rotating frame of reference. We show that rotating quantum turbulence is fundamentally different from its classical counterpart. While it displays, as in the classical case at moderate rotation rates, an inverse cascade of energy at large scales, at small scales it displays an anisotropic emission of waves and an energy scaling compatible with the ultraquantum turbulence regime.

## II. METHODS

### A. Rotating Gross-Pitaevskii equation

We solve numerically the Gross-Pitaevskii equation (GPE) with a trapping potential $V(\mathbf{r})$ in a rotating frame of reference. The rotating Gross-Pitaevskii equation (RGPE), which describes the evolution of a zero-temperature condensate of weakly interacting bosons of mass $m$ under this conditions, is

$$i\hbar\frac{\partial\psi(\mathbf{r},t)}{\partial t}=\left[-\frac{\hbar^2\nabla^2}{2m}+g|\psi(\mathbf{r},t)|^2+V(\mathbf{r})-\Omega J_z\right]\psi(\mathbf{r},t), \tag{1}$$

where $g$ is related to the scattering length, $\Omega$ is the rotation angular velocity along $z$, and $J_z$ is the angular momentum operator. This equation can be obtained from the usual GPE by applying the constant-speed time-dependent rotation operator $R(t,\Omega)$ and redefining the order parameter in the rotating frame as $\psi=R(t,\Omega)\psi'$, where $\psi'$ is the wave function in the nonrotating frame.

By means of the Madelung transformation [6], this equation can be mapped to the Euler equation for an isentropic, compressible, and irrotational fluid in the nonrotating frame of reference with an extra quantum pressure term. The transformation is given by

$$\psi'(\mathbf{r},t)=\sqrt{\rho(\mathbf{r},t)/m}e^{iS(\mathbf{r},t)}, \tag{2}$$

where $\rho(\mathbf{r},t)$ is the fluid mass density and $S(\mathbf{r},t)$ is the phase of the order parameter such that the fluid velocity in the nonrotating frame is $\mathbf{v}=(\hbar/m)\nabla S(\mathbf{r},t)$. The resulting flow is thus irrotational except for topological defects where the vorticity is quantized so that $\oint_{\mathcal{C}}\mathbf{v}\cdot d\mathbf{l}=(2\pi\hbar/m)n$, with $n\in\mathbb{N}$, and where $\Gamma_0=2\pi\hbar/m$ is the quantum of circulation. In the rotating frame, the velocity is given by $\mathbf{v}_R=(\hbar/m)\nabla S(\mathbf{r},t)-\Omega\hat{z}\times\mathbf{r}$. Replacing this velocity in the Euler equation or equivalently applying a Madelung transformation to Eq. (1) results in the Euler equation for the fluid in the rotating frame, with the extra Coriolis and centrifugal forces (see also [36]).

Note that while classical rotating turbulence is typically studied in incompressible regimes [28,33], BECs are diluted gases and compressibility cannot be neglected. Nevertheless, the weakly compressible case (which goes beyond the cases considered in this study) could be of interest for the large-scale dynamics of superfluid helium.

### B. Waves in the nonrotating system

In the absence of rotation and for $V(\mathbf{r})=0$, Eq. (1) becomes the usual GPE. If this equation is linearized around an equilibrium with uniform mass density $\rho$, one finds the Bogoliubov dispersion relation for sound waves

$$\omega_B(k)=ck\sqrt{1+(\xi k)^2/2}, \tag{3}$$

where $c=(g\rho/m)^{1/2}$ and $\xi=\hbar/(2gm\rho)^{1/2}$ are the uniform sound speed and coherence length, respectively [37].

In the presence of quantized vortices, using the Biot-Savart law, one can find normal modes of the vortex deformation. These correspond to a set of helicoidal Kelvin waves with the dispersion relation

$$\omega_K(k_\parallel)=\frac{2c\xi}{\sqrt{2}r_n^2}\left(1\pm\sqrt{1+k_\parallel r_n\frac{K_0(k_\parallel r_n)}{K_1(k_\parallel r_n)}}\right), \tag{4}$$

where $r_n$ is the vortex radius, $K_0$ and $K_1$ are modified Bessel functions, and $k_\parallel$ is the wave number along the direction of the vortex core. The radius $r_n$ can be estimated using theoretical arguments or directly from the density profile in experiments or simulations and is approximately equal to $2\xi$ [6,9,24]. Typically, the random orientation of quantized vortices in a BEC results in a dependence of Eq. (4) on $k$ instead of $k_\parallel$. The presence of rotation will align vortices preferentially along $z$, making $k_\parallel=k_z$. Finally, note that this dispersion relation is the same as the classical one derived by Kelvin but dependent on the quantum of circulation $\Gamma_0=2\sqrt{2}\pi c\xi$ instead of on the circulation associated with the total flow vorticity.

### C. Waves in the rotating system

The presence of rotation modifies the system behavior. Above a threshold in $\Omega$, $\Omega_c=(5\hbar/2mR_\perp^2)\ln(R_\perp/\xi)$ (where $R_\perp$ is the condensate radius), the flow tries to mimic a solid-body rotation [20]. As a result of the quantization, the flow can only accomplish this by generating a regular array of quantized vortices such that their total circulation equals that of the rotation. The array is known as the Abrikosov lattice, forcing the system into a 2D state. To obtain a solid-body-like rotation, the density of vortices per unit area must be $n_v=\Omega/\sqrt{2}\pi c\xi$. Tkachenko [23] found that for an infinite system [$V(\mathbf{r})=0$] this lattice must be triangular to minimize the free energy. When perturbed, this lattice has normal modes called Tkachenko waves. For the triangular lattice the modes follow the dispersion relation

$$\omega_T^2=\frac{2C_2}{\rho m}\frac{c^2k^4}{4\Omega^2+[4(C_1+C_2)/\rho m]k^2}, \tag{5}$$

where $C_1$ is the compressional modulus and $C_2$ the shear modulus of the vortex lattice [38]. There are two Thomas-Fermi limits for this expression. The so-called rigid limit corresponds to small $\Omega$ compared to the lowest compression frequency $ck_0$, where $k_0$ corresponds to the fundamental mode of the trap. The soft limit corresponds to $\Omega$ larger than $ck_0$, but smaller than $mc^2/\hbar$. In this regime, the vortex radius is smaller than the intervortex distance and compressibility cannot be neglected. This is the regime we consider in this study, whose dispersion relation can be approximated as ($\gamma\approx 4$) [38]

$$\omega_T^{(s)}=\left[\left(1-\gamma\frac{\sqrt{2}\Omega\xi}{c}\right)\frac{\xi c^3}{8\sqrt{2}\Omega}\right]^{1/2}k^2. \tag{6}$$

Both the Abrikosov lattice and Tkachenko waves were experimentally observed in previous studies, such as [1].

Although there are no laboratory studies of rotating quantum turbulence in BECs, vortex lattices were observed as metastable states in numerical simulations of rotating classical turbulence in finite domains [32].

The Kelvin dispersion relation also suffers a modification in the presence of rotation. For a single quantized vortex in the rotating frame it becomes

$$\omega_K^{(\mathrm{r})} = \Omega + \omega_K(k_\parallel). \tag{7}$$

For many vortices, the presence of the vortex lattice also affects this dispersion relation; expressions taking into account this effect can be found in [24].

### D. Energy, momentum, and vortex length

From the energy functional that defines the RGPE, the total energy can be decomposed as $E = E_k + E_q + E_p + E_V + E_{\mathrm{rot}}$, with kinetic energy $E_k = \langle \rho v^2\rangle/2$, quantum energy $E_q = (\hbar^2/2m^2)\langle(\nabla\sqrt{\rho})^2\rangle$, internal (or potential) energy $E_p = (g/2m^2)\langle\rho^2\rangle$, trap potential energy $E_{\mathrm{V}} = \langle V\rho\rangle$, and rotation energy $E_{\mathrm{rot}} = -\Omega\langle\psi^* J_z\psi\rangle$. In all cases, the angular brackets denote volume average. Using the Helmholtz decomposition $\sqrt{\rho}\mathbf{v} = (\sqrt{\rho}\mathbf{v})^{(\mathrm{c})} + (\sqrt{\rho}\mathbf{v})^{(\mathrm{i})}$ [6], where the superindices c and i denote the compressible and incompressible parts, respectively [i.e., such that $\nabla\cdot(\sqrt{\rho}\mathbf{v})^{(\mathrm{i})} = 0$], the kinetic energy can be further decomposed into the compressible $E_{\mathrm{k}}^{\mathrm{c}}$ and incompressible $E_{\mathrm{k}}^{\mathrm{i}}$ kinetic energy components. It is worth pointing out that this decomposition is used in classical compressible flows [39]. For each energy, using Parseval's identity, we can build spatial spectra and spatiotemporal spectra [9].

Another quantity of interest is the incompressible momentum spectrum $P^{(\mathrm{i})}(k)$ [6]. It has been seen empirically that in many flows and for sufficiently large wave numbers, $P^{(\mathrm{i})}(k)$ can be obtained from the momentum spectrum per vortex unit length of a single quantized vortex $P_s^{(\mathrm{i})}(k)$, summing it as many times as the number of vortices in the system times their lengths [6,10]. Thus, the total vortex length $L_v$ can be estimated as

$$\frac{L_v}{2\pi} = \frac{\int_{k_{\mathrm{min}}}^{k_{\mathrm{max}}} P^{(\mathrm{i})}(k)dk}{\int_{k_{\mathrm{min}}}^{k_{\mathrm{max}}} P_s^{(\mathrm{i})}(k)dk}, \tag{8}$$

where $k_{\mathrm{min}}$ is a cutoff ($k_{\mathrm{min}} = 10$ in this study, as the contribution from smaller wave numbers is dominated by the trap geometry) and $k_{\mathrm{max}}$ is the maximum resolved wave number. From $L_v$, the mean intervortex distance is $\ell = (\mathcal{V}/L_v)^{1/2}$, where $\mathcal{V}$ is the condensate volume.

### E. Numerical simulations

We solve Eq. (1) under an axisymmetric potential $V(\mathbf{r}) = m\omega_\perp^2(x^2+y^2)/2$, in a cubic domain with periodic boundary conditions along the rotation axis. The choice of the axisymmetric potential corresponds to the elongated limit of a cigar-shaped trap and is chosen to limit the contamination of the trap geometry in the computation of axisymmetric turbulent quantities. We use a Fourier-based pseudospectral method with $N^3 = 512^3$ spatial grid points and the 2/3 rule for dealiasing, and a fourth-order Runge-Kutta method to evolve the equations in time, using the parallel code GHOST, which is publicly available [40], in a cubic domain of size $[-\pi,\pi]L \times [-\pi,\pi]L \times [-\pi,\pi]L$ so that the edges have length $2\pi L$. To accommodate the nonperiodic potential and angular momentum operator $J_z = x\partial_y - y\partial_x$ in the Fourier base in $x$ and $y$, we smoothly extend these functions to make them (and all their spatial derivatives) periodic [41], in a region far away from the trap center such that the gas density in that region is negligible. This also prevents the occurrence of the Gibbs phenomenon near the domain boundaries. To do so, a convolution between the Fourier transform of $V(\mathbf{r})$ or $J_z$ and a Gaussian filter in $k_x$ and $k_y$ is computed. The width of the filter is chosen empirically to minimize errors in $V(\mathbf{r})$ and in $J_z$ in the region occupied by the condensate. In practice we use a width $\sigma = N\Delta k/17$, where $\Delta k$ is the resolution in wave-number space. With this choice, errors in the computation of $V(\mathbf{r})$ and $J_z$ are almost constant and approximately equal to $10^{-7}$ in the region occupied by the condensate. Values of $\omega_\perp$ are also chosen to keep the condensate confined in the region of the $xy$ plane satisfying these errors.

In the following we use dimensionless units. All parameters are obtained by setting $c_0 = (g\rho_0/m)^{1/2} = 2U$ and $\xi_0 = \hbar/(2gm\rho_0)^{1/2} = 0.017L$, both defined using the reference mass density in the center of the trap $\rho_0 = 1M/L^3$. These quantities are scaled with a unitary length $L$, a mass $M$, and a typical speed $U$. Considering typical dimensional values in experiments with $L \approx 10^{-4}$ m and $c_0 \approx 2\times10^{-1}$ m/s [4], this results in $\xi_0 \approx 1.7\times10^{-6}$ m [for the dispersion relations shown below, the relations in Secs. II B and II C are evaluated using mean values for $c$ and $\xi$ in the condensate, obtained from the mean mass density in the trap with $\Omega = 0$, $\langle\rho(\mathbf{r},t)\rangle_{\Omega=0}$].

It is important to note that we must prepare the system in a disordered initial state to have turbulence. Without such an initial state, a nonrotating condensate should result in an equilibrium without quantized vortices and a rotating condensate (with $\Omega > \Omega_c$) should result in an Abrikosov lattice. Moreover, none of these states can be readily accessed from the decay of the GPE or RGPE without proper initial conditions, as these equations have no dissipation (see, e.g., [42]). To obtain a turbulent state, we thus perturb an initial Gaussian density profile with a three-dimensional and random arrangement of vortices using the initial conditions described in [11] such that the kinetic energy spectrum peaks initially at $k \approx 5$ (i.e., approximately 1/5 of the domain size, leaving room in spectral space for self-organization processes). To reduce the emission of phonons and to let the system decay into an initial condition compatible with the RGPE, we integrate this initial state to a steady state using a rotating real advective Landau-Ginzburg equation, which can be derived from Eq. (1) following the method described in [6] for the nonrotating case. The equation is

$$\frac{\partial\psi}{\partial t} = \left[\frac{\hbar\nabla^2}{2m} - \frac{g}{\hbar}|\psi|^2 - \frac{V}{\hbar} + \frac{\Omega J_z}{\hbar} + \mu - i\mathbf{v}\cdot\nabla - \frac{m|\mathbf{v}|^2}{2\hbar}\right]\psi, \tag{9}$$

where $\mu$ is the chemical potential and $\mathbf{v}$ the velocity field generated by the random arrangement of vortices. Note this equation corresponds just to the imaginary-time propagation of the RGPE, with a local Galilean transformation corresponding to the flow $\mathbf{v}$. The final state of this equation is then used

TABLE I. Parameters of all simulations: $\Omega$ is the rotation angular velocity, $\Omega/\omega_\perp$ is the ratio of $\Omega$ to the frequency of the potential, $\Gamma_\Omega/\Gamma_0$ is the ratio of the circulation in $\Omega$ to the quantum of circulation, $\Omega/\Omega_c$ is the ratio of $\Omega$ to the critical value $\Omega_c$, $\ell/R_\perp$ is the ratio of the intervortex length to the condensate radius, and Ro is the Rossby number.

| $\Omega$ $(U/L)$ | $\Omega/\omega_\perp$ | $\Gamma_\Omega/\Gamma_0$ | $\Omega/\Omega_c$ | $\ell/R_\perp$ | Ro |
|---|---|---|---|---|---|
| 0 | 0 | 0 | 0 | 0.47 | |
| 0.6 | 0.29 | 12.6 | 2.27 | 0.55 | $6.9\times10^{-2}$ |
| 0.8 | 0.37 | 16.8 | 3.03 | 0.44 | $5.6\times10^{-2}$ |
| 1.0 | 0.47 | 23.0 | 4.12 | 0.31 | $5.4\times10^{-2}$ |
| 1.2 | 0.60 | 38.4 | 6.63 | 0.39 | $7.5\times10^{-2}$ |
| 1.3 | 0.55 | 27.8 | 5.02 | 0.48 | $5.1\times10^{-2}$ |
| 1.5 | 0.56 | 25.1 | 4.66 | 0.31 | $4.5\times10^{-2}$ |

as the initial condition for the RGPE. If we do not want a turbulent initial state (e.g., to get an Abrikosov lattice), we can integrate this equation with an initial Gaussian density profile and $\mathbf{v} = 0$.

Table I lists the parameters of all simulations. As already mentioned, the value of $\omega_\perp$ is varied with $\Omega$ to keep $R_\perp$ more or less the same. In all cases $\Omega/\omega_\perp \leqslant 0.6$, indicating the system is in or near a mean-field Thomas-Fermi regime [20,25,43], except when $\Omega = 0$, $\Omega > \Omega_c$ (i.e., in the absence of turbulence the system displays a steady state with an Abrikosov lattice), and the circulation associated with the rotation $\Gamma_\Omega = \int \Omega\, dS$ is much larger than $\Gamma_0$. The intervortex distance is smaller than $R_\perp$ (the ratio $\ell/R_\perp$ is often accessible in experiments [1]) and a Rossby number defined as $\mathrm{Ro} = u'/2\Omega R_\perp$ (with $u'$ the rms velocity in the rotating frame), which measures the inverse of the strength of rotation in classical turbulence, is small in all our rotating BECs.

## III. RESULTS

### A. Inverse energy cascade

Figure 1 shows the time evolution of several energy components for the simulations with $\Omega = 0$ and 1.2. All energy components display oscillations independently of $\Omega$, which are associated with a breathing mode of the condensate in the trap (indeed, we verified that this frequency is proportional to $2\omega_\perp$, as expected for such mode [44]). Looking at the slow evolution, for $\Omega = 0$ the incompressible kinetic energy decreases while the compressible and quantum energy increase. This is the result of the free decay of the turbulence: The incompressible kinetic energy is transferred towards smaller scales and dissipated as sound waves. This results in the increase of energy in compressible motions and in an increase of inhomogeneities which increase the quantum pressure. However, for $\Omega = 1.2$ all energy components oscillate around a mean and approximately constant value, with a very small increase of the quantum energy at early times. This indicates that less energy in the flow is being dissipated. Where is this energy going?

As shown in Fig. 2, in the presence of rotation energy accumulates more and more at the largest available scale. The figure shows the time evolution of the incompressible kinetic energy at the gravest mode ($k = 1$) in all simulations. Leaving

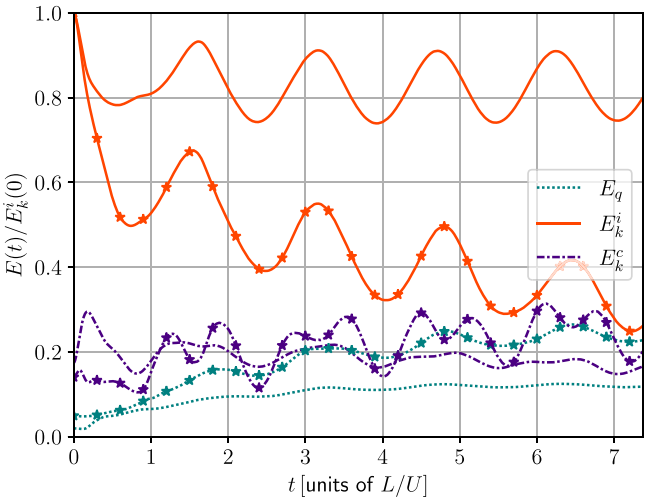


FIG. 1. Time evolution of the compressible, incompressible, and quantum energy for two simulations (with $\Omega = 0$ for the lines with stars and $\Omega = 1.2$ for the lines without markers). All energies are normalized by the initial ($t = 0$) incompressible kinetic energy of each simulation.

aside the oscillations, note that for $\Omega = 0$ energy in this mode decays slowly, while for $\Omega > 0$, the stronger the rotation is, the more the energy in this mode increases with time. In other words, the energy initially at $k \approx 5$ is transferred to the $k = 1$ mode (i.e., to larger scales) instead of to larger wave numbers (smaller scales). As a result, less of the kinetic energy in the turbulent flow is available for dissipation as sound waves. This results from the quasi-two-dimensionalization of the flow in the presence of rotation, which results in an inverse energy cascade even in quantum turbulence [11] or equivalently in the condensation of the kinetic energy at the largest available scale in a process akin to Onsager's negative temperature states of an ideal gas of 2D point vortices [45,46]. Thus, the first distinguishing feature of rotating quantum turbulence is its spontaneous evolution towards negative temperature states

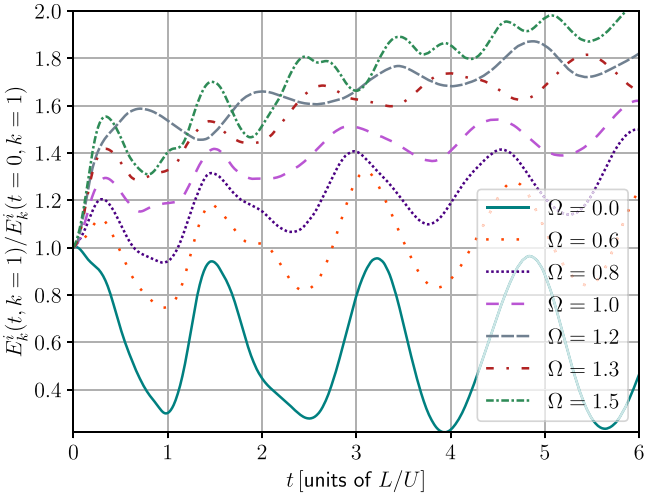


FIG. 2. Incompressible kinetic energy at $k = 1$ in all simulations, normalized by the initial ($t = 0$) incompressible kinetic energy in the same Fourier shell.

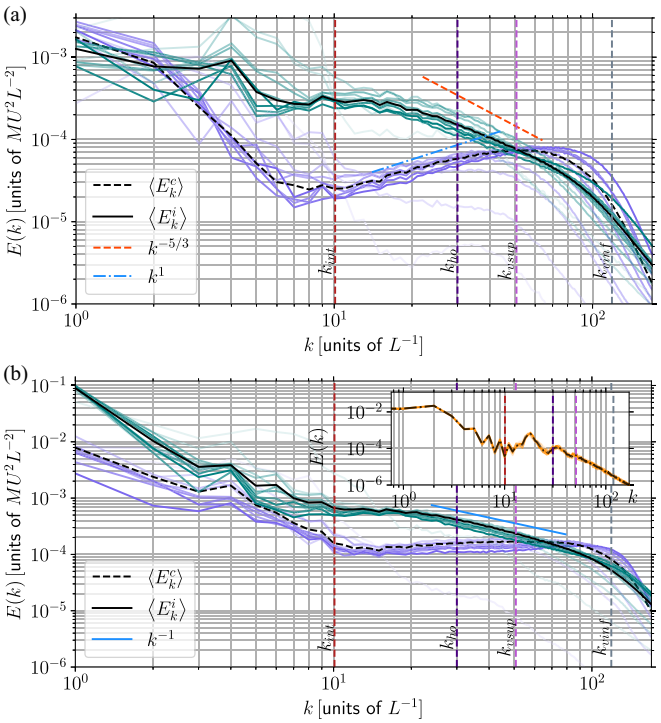


FIG. 3. Incompressible (green, top curves at $k = 10$ surrounding the time average with the black solid line) and compressible (purple, bottom curves at $k = 10$ surrounding the time average with the black dashed line) kinetic energy spectra at different times (from light to dark as time evolves and the time average over 2.5 breathing-mode oscillations indicated with black lines) in a condensate with (a) $\Omega = 0$ and (b) $\Omega = 1.2$. Several power laws are indicated as references by solid lines. The inset shows the incompressible kinetic energy spectrum of an Abrikosov lattice (i.e., a nonturbulent stationary solution). In all panels, vertical lines show characteristic wave numbers: $k_{\rm int}$, associated with the intervortex distance; $k_{\rm ho}$, associated with the condensate size for a noninteracting gas; and $k_{\rm vinf}$ and $k_{\rm vsup}$, associated with two measures of the intravortex scale.

without the need for a change in the dimensionality of the trap.

The inverse energy cascade can be further confirmed in the spatial spectra in Fig. 3, which shows the incompressible and compressible kinetic energy spectra at different times in the simulations with $\Omega = 0$ and 1.2. While in the former case the incompressible spectrum peaks at all times at $k = 4$, in the latter the same spectrum peaks at the smallest available wave number.

### B. Direct cascade subrange

For wave numbers $k > 5$, the spectra in Fig. 3 display distinct power laws. When $\Omega = 0$, the incompressible kinetic energy displays a range compatible with Kolmogorov $\sim k^{-5/3}$ scaling. The compressible kinetic energy displays an $\sim k^1$ scaling compatible with an axisymmetric (2D) thermalization, probably associated with the trap geometry. However, for $\Omega = 1.2$ the spectra are very different. The incompressible direct cascade subrange is compatible with $\sim k^{-1}$ scaling, as in Vinen or ultraquantum turbulence. The inset in Fig. 3 also shows as a reference the incompressible kinetic spectrum of

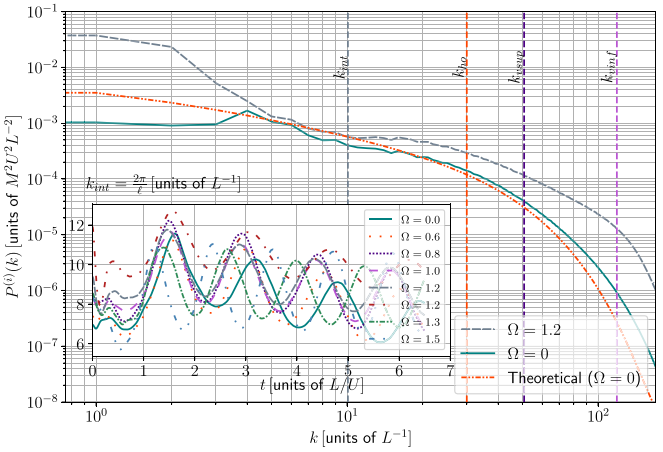


FIG. 4. Momentum spectrum for $\Omega = 0$ and 1.2, compared with the theoretical momentum spectrum per unit length of one vortex [6], multiplied by the total vortex length in the simulation with $\Omega = 0$. The inset shows the intervortex wave number as a function of time for all simulations.

an Abrikosov lattice with $\Omega = 1.2$ (i.e., of a nonturbulent stationary solution of the RGPE), to show that its spectrum displays characteristic peaks and no clear $\sim k^{-1}$ scaling. The compressible kinetic spectrum in the rotating turbulent regime also changes its scaling and becomes flatter, as if the energy in sound modes reaches one-dimensional equipartition. As references, the figure also shows four characteristic, averaged in time, wave numbers: the intervortex wave number $k_{\rm int} = 2\pi/\ell$, the inverse harmonic trap length $k_{\rm ho}$ for noninteracting bosons [47], and $k_{\rm vsup}$ and $k_{\rm vinf}$, which correspond to the inverse lengths at which a single isolated vortex recovers 0.9 and 0.5, respectively, of the mass density $\rho_0$ for $\Omega = 0$. The direct cascade subranges take place for $k > k_{\rm int}$ and $k < k_{\rm vinf}$, and the direct $\sim k^{-1}$ scaling obtained with rotation is very different from the $\sim k^{-2}$ scaling observed in rotating classical turbulence [28–30].

A $k^{-1}$ scaling has been associated before with the presence of a counterflow [12], with fluxless solutions [48], or with disorganized vortex tangles [19,49]. In our case, the flux of energy towards small scales in the presence of rotation is substantially decreased, as evidenced by the accumulation of energy at large scales and also by direct computation of the flux (not shown). Also, the vortex tangles in the flow in the presence of rotation change drastically. This is shown in Fig. 4, which shows the spectrum of momentum $P^{(\rm i)}(k)$ for $\Omega = 0$ and 1.2, together with a theoretical estimation of the spectrum for a superposition of individual quantized vortices with the same total length (for $\Omega = 0$). For $\Omega = 0$ the shapes of the theoretical and observed momentum spectra are similar for $k \gtrsim 5$, but very different for $\Omega = 1.2$. This indicates that the vortex bundles indeed change in the presence of rotation. Differences at large scales (associated with the flow and trap geometry) can be expected in all cases; note in particular the excess of momentum at small wave numbers for $\Omega = 1.2$, which again confirms the large-scale self-organization. Differences at the smaller scales ($k > k_{\rm ho}$) may be the result of contributions coming from the momentum field $\rho\mathbf{v}$ at the boundary of the condensed cloud. Indeed, in the presence of

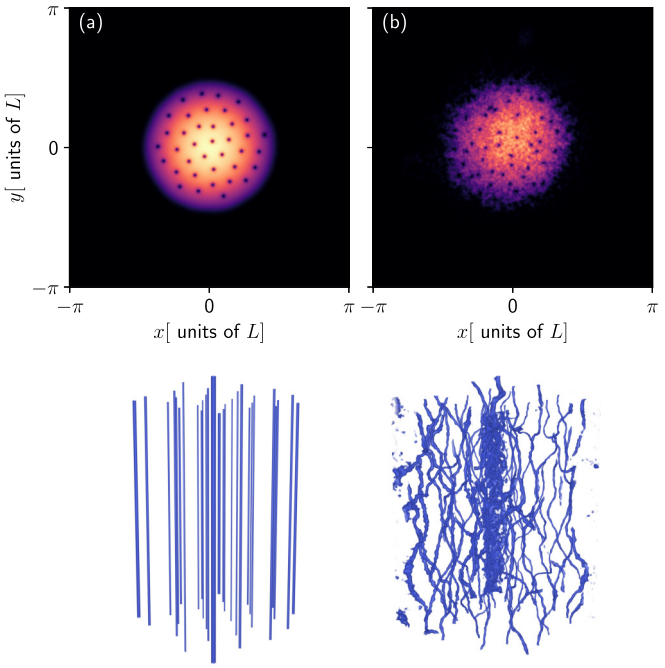


FIG. 5. Density $\rho(x, y, z = \pi L)$ (top) and three-dimensional volume rendering of quantized vortices in the central region of the trap (bottom) for simulations with $\Omega = 1.2$ at late times in (a) a stationary regime and (b) the turbulent regime. Volume renderings were done using the software VAPOR [50].

rotation there must be a net circulation generated by the vortex tangle in the condensate, which should be balanced with the circulation in a boundary layer. The inset in Fig. 4 shows the evolution of $k_{\rm int}$ over time, calculated from the momentum spectrum. In all cases, on top of the breathing-mode oscillations, there is an initial increase of $k_{\rm int}$ (and thus of $L_v$, the total vortex length) associated with vortex stretching.

However, unlike homogeneous quantum turbulence, the $\sim k^{-1}$ scaling of the incompressible kinetic energy in the rotating case cannot be the result of unpolarized bundles of vortices (i.e., of randomly and independently oriented vortices [19,49]). As explained before, the vortices in the rotating BEC must be polarized and more or less aligned in order to approximate the solid-body rotation. This is illustrated in Fig. 5, which shows a horizontal cut of the mass density and a 3D volume rendering of quantized vortices for an Abrikosov lattice (i.e., in the nonturbulent stationary solution) and for the turbulent regime ($\Omega = 1.2$). The latter system tries to mimic the former, with a quasi-2D bundle of vortices, albeit with disorder in the vortices' positions as well as with deformation in the $z$ direction (the axis of rotation). The $\sim k^{-1}$ scaling can thus be the result of the disorder in a quasi-2D system. Let us define $\mathbf{u}(\mathbf{r}) = (\sqrt{\rho}\mathbf{v})^{(\rm i)}$. The Fourier transform of the incompressible field generated by many quantum vortices can be written, using the translation operator, as $\hat{\mathbf{u}}(k) = \sum_j e^{-i\mathbf{k}\cdot\mathbf{r}_j}\hat{\mathbf{u}}_v(k)$, where $\hat{\mathbf{u}}_v(k)$ is the Fourier transform of the incompressible field generated by just one quantized vortex and $\mathbf{r}_j$ the position of the $j$th vortex. Then the power spectrum of $\mathbf{u}$ is the angle average in Fourier space of

$$\hat{\mathbf{u}}^*(\mathbf{k}) \cdot \hat{\mathbf{u}}(\mathbf{k}) = \sum_{ij} e^{-i\mathbf{k}\cdot(\mathbf{r}_i - \mathbf{r}_j)} |\hat{\mathbf{u}}_v(\mathbf{k})|^2, \tag{10}$$

where the asterisk denotes a complex conjugate. If the vortices are organized in a lattice, the spectrum is dominated by the lattice spatial ordering (as in the inset in Fig. 3). However, for a disorganized state with random positions, the sum in Eq. (10) reduces to the sum of the spectra of individual vortices, each with an $\sim k^{-1}$ scaling [6,19].

### C. Wave emission

In nonrotating quantum turbulence, energy is transferred towards smaller scales through vortex reconnection and a Kelvin wave cascade [7] and is finally dissipated through

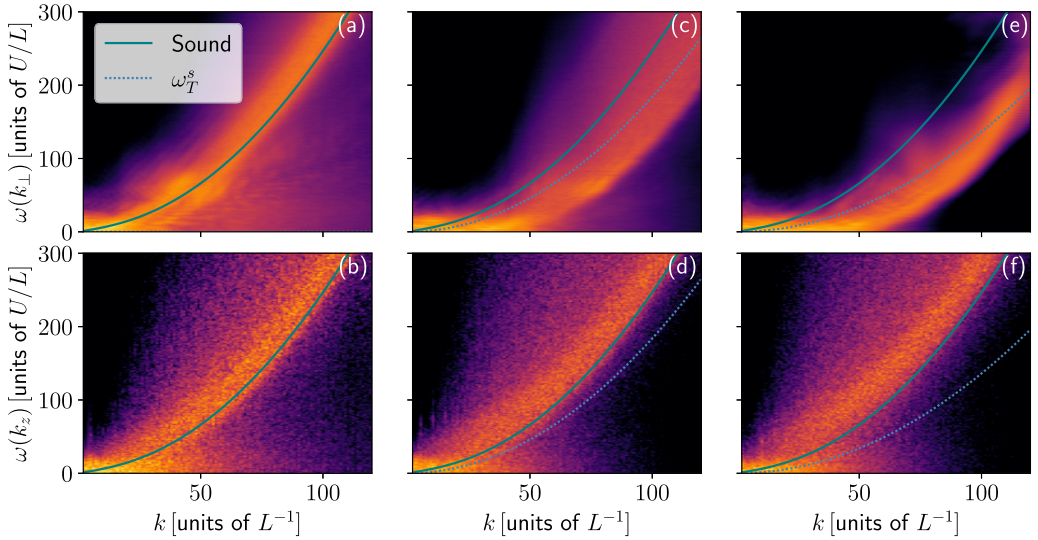


FIG. 6. Spatiotemporal mass spectra for simulations with increasing $\Omega$, as a function of (a), (c), and (e) $k_\perp$ (for $k_z = 0$) and (b), (d), and (f) $k_z$ (for $k_x = k_y = 0$) for (a) and (b) $\Omega = 0$, (c) and (d) $\Omega = 1$, and (e) and (f) $\Omega = 1.2$. As a reference, the dispersion relations of sound and soft Tkachenko waves are shown as a reference.

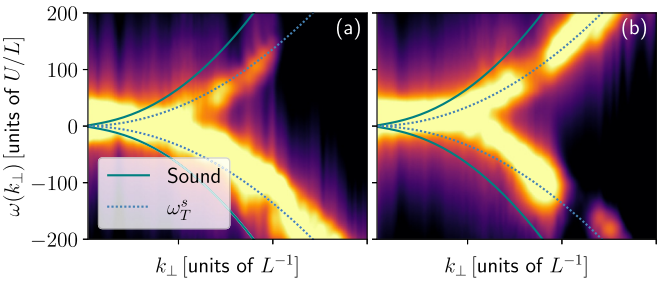


FIG. 7. Spatiotemporal mass spectrum for $\Omega = 1.2$ as a function of $k_\perp$ (for $k_z = 0$) centered at two different times: (a) corresponds to time $t = 0.32$ and (b) corresponds to time $t = 3.68$. Note the pulsation between the positive and negative $\omega$ branches, as a mode moves outward or inward. As a reference, sound and soft Tkachenko dispersion relations are shown.

sound emission [51,52]. The study of the waves excited by these flows can shed light on how energy is dissipated in the presence of rotation and on the reasons for the different scaling laws observed in Fig. 3.

Figure 6 shows the mass spatiotemporal spectrum [9] as a function of the frequency $\omega$, of $k_\perp = (k_x^2 + k_y^2)^{1/2}$ (for $k_z = 0$), or of $k_z$ (for $k_\perp = 0$), for $\Omega = 0$, 1, and 1.2. Figures 6(a) and 6(b) show these spectra when $\Omega = 0$. Excitations accumulate near the dispersion relation of sound waves. When $\Omega$ increases, emission of waves changes drastically. In $k_z$, excitations still accumulate around sound waves: Turbulence dissipates energy by emitting sound in the $z$ direction. However, in $k_\perp$ the dispersion relation shifts towards larger values of $k_\perp$ as $\Omega$ increases [Figs. 6(c) and 6(e)] and become closer to soft Tkachenko waves.

These modes in $k_\perp$ are not stationary. Figure 7 shows two spatiotemporal mass spectra as a function of $k_\perp$ in the simulation with $\Omega = 1.2$, for both positive and negative frequencies. Note the pulsation between positive and negative $\omega(k_\perp)$ branches as time evolves. In other words, modes are of the form $\exp[i(\mathbf{k}_\perp \cdot \mathbf{r}_\perp - \omega t)]$ and $\exp[i(\mathbf{k}_\perp \cdot \mathbf{r}_\perp + \omega t)]$, respectively, or equivalently the modes collectively propagate outward or inward. Interestingly, the alternation of energy between the positive and negative $\omega(k_\perp)$ branches is not visible in the simulation with $\Omega = 0$. Thus, it must represent a global deformation of the vortex lattice on top of which turbulence develops (and also feeds with energy), the breathing mode possibly being part of it, and which can give a mechanism

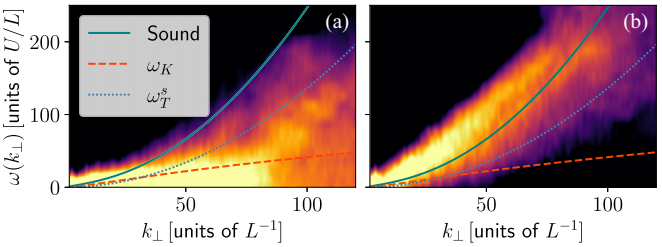


FIG. 8. Spatiotemporal spectrum of (a) the incompressible kinetic energy $E_k^{(\mathrm{i})}(k_\perp, \omega)$ and (b) the compressible energy $E_k^{(\mathrm{c})}(k_\perp, \omega)$ (for $k_z = 0$) in a condensate with $\Omega = 1.2$. As a reference sound, soft Tkachenko wave and Kelvin wave dispersion relations are shown. The solid-body mean rotation is removed from these spectra.

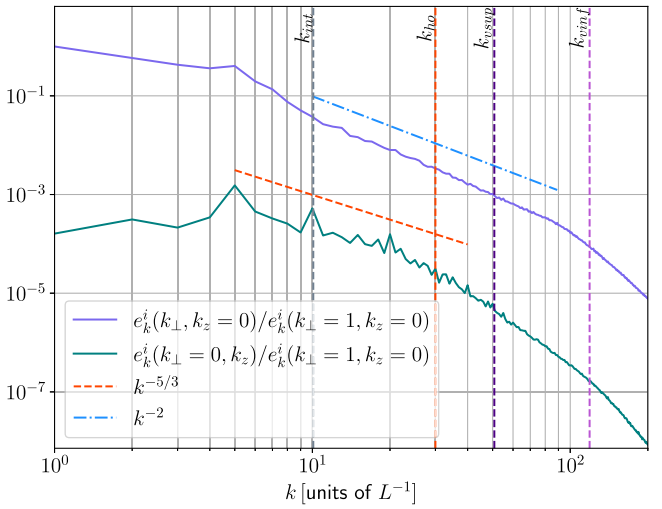


FIG. 9. Incompressible kinetic energy spectrum (for $\Omega = 1.2$) as a function of $k_\perp$ for modes with $k_z = 0$ (top spectrum) and as a function of $k_z$ for modes with $k_\perp = 0$ (bottom spectrum), normalized by the incompressible energy in $(k_\perp = 1, k_z = 0)$. Power laws and characteristic wave numbers are indicated as references.

for energy dissipation as vortices move through this pulsation (i.e., it could act as an effective counterflow).

Waves manifest not only in the mass spatiotemporal spectrum. The spatiotemporal spectra of the incompressible and compressible kinetic energies as a function of $k_\perp$ (for $k_z = 0$) are shown in Fig. 8, computed after turbulence is totally developed and over half a breathing-mode period. The spectra are computed after removing the solid-body rotation. The incompressible energy shows excitations at lower frequencies, near the Kelvin and soft Tkachenko dispersion relations, and with excitations at frequencies close to the soft Tkachenko modes observed in the mass spectrum in Fig. 6, suggesting these modes correspond in part to inward or outward incompressible deformations. In the compressible energy, excitations are approximately compatible with sound modes and with some power in Tkachenko frequencies.

Anisotropic sound (or compressible mode) emission was observed in experiments of nonturbulent rotating BECs [53]. In our case they seem to provide different mechanisms for the energy dissipation, along different directions in spectral space. Figure 9 shows the incompressible kinetic spectrum $e_k^{(\mathrm{i})}(k_\perp, k_z)$ for modes with $k_\perp = 0$ or $k_z = 0$ and for $\Omega = 1.2$. These spectra can be computed from the full spatiotemporal spectrum $E_k^{(\mathrm{i})}(\mathbf{k}, \omega)$ by integrating over all frequencies. In the direction of $k_\perp$ the spectrum displays a scaling compatible with $\sim k_\perp^{-2}$ in a broad range of wave numbers (compatible with predictions from the theory of classical rotating turbulence [33]), while along $k_z$ the spectrum displays an $\sim k_z^{-5/3}$ compatible scaling. This scaling is visible at wave numbers above and below the intervortex wave number and thus is probably the result of vortex reconnection with some contribution of a Kelvin wave cascade.

## IV. CONCLUSION

Rotating quantum turbulence is fundamentally different from both nonrotating quantum turbulence and classical rotat-

ing turbulence. The quasi-two-dimensionalization of the flow results in an inverse energy transfer, as in quasi-2D quantum turbulence [11] and in classical rotating turbulence [31]. This inverse transfer can be also interpreted as a negative temperature state, as predicted for 2D point vortices [54] and observed in BEC experiments [45,46]. However, the small scales display a scaling different from all other regimes.

An $\sim k^{-1}$ power law at intermediate wave numbers in the incompressible kinetic energy is reminiscent of the scaling of Vinen turbulence, albeit in this case there is no obvious counterflow in the system. However, the system displays very little transfer of energy to small scales (most kinetic energy is transferred to larger scales) and a different arrangement of quantized vortices. This, together with a pulsation of the condensate inward and outward (with the associated friction of the vortices with this flow), can provide a way for the system to dissipate energy in the perpendicular direction as suggested by the spatiotemporal spectra. Along the axis of rotation, energy is dissipated instead as sound waves. This results in a thermalization of one-dimensional sound modes, with a flat spectrum of the compressible kinetic energy, and distinct scaling of the incompressible energy when individual modes are studied: an $\sim k_z^{-5/3}$ subdominant scaling for modes with $k_\perp = 0$ and an $\sim k_\perp^{-2}$ dominant scaling for modes with $k_z = 0$. A similar mechanism may be also present in recent simulations of quantum turbulence in BECs [17,18], in which cigar-shaped traps and a few multicharged aligned vortices are studied.

## ACKNOWLEDGMENTS

J.A.E. and P.D.M. acknowledge financial support from UBACYT Grant No. 20020170100508BA and ANPCyT PICT Grant No. 2018-4298. M.E.B. acknowledges support from the French Agence Nationale de la Recherche (ANR QUTE-HPC Project No. ANR-18-CE46-0013).

[1] I. Coddington, P. Engels, V. Schweikhard, and E. A. Cornell, Phys. Rev. Lett. **91**, 100402 (2003).
[2] G. P. Bewley, D. P. Lathrop, and K. R. Sreenivasan, Nature (London) **441**, 588 (2006).
[3] E. A. L. Henn, J. A. Seman, G. Roati, K. M. F. Magalhães, and V. S. Bagnato, Phys. Rev. Lett. **103**, 045301 (2009).
[4] A. C. White, B. P. Anderson, and V. S. Bagnato, Proc. Natl. Acad. Sci. USA **111**, 4719 (2014).
[5] M. C. Tsatsos, P. E. Tavares, A. Cidrim, A. R. Fritsch, M. A. Caracanhas, F. E. A. dos Santos, C. F. Barenghi, and V. S. Bagnato, Phys. Rep. **622**, 1 (2016).
[6] C. Nore, M. Abid, and M. E. Brachet, Phys. Fluids **9**, 2644 (1997).
[7] V. S. L'vov and S. Nazarenko, JETP Lett. **91**, 428 (2010).
[8] J. Laurie, V. S. L'vov, S. Nazarenko, and O. Rudenko, Phys. Rev. B **81**, 104526 (2010).
[9] P. Clark di Leoni, P. D. Mininni, and M. E. Brachet, Phys. Rev. A **92**, 063632 (2015).
[10] V. Shukla, P. D. Mininni, G. Krstulovic, P. Clark di Leoni, and M. E. Brachet, Phys. Rev. A **99**, 043605 (2019).
[11] N. P. Müller, M.-E. Brachet, A. Alexakis, and P. D. Mininni, Phys. Rev. Lett. **124**, 134501 (2020).
[12] W. F. Vinen, Proc. R. Soc. London Ser. A **240**, 114 (1957).
[13] P. M. Walmsley and A. I. Golov, Phys. Rev. Lett. **100**, 245301 (2008).
[14] C. F. Barenghi, L. Skrbek, and K. R. Sreenivasan, Proc. Natl. Acad. Sci. USA **111**, 4647 (2014).
[15] A. W. Baggaley, C. F. Barenghi, and Y. A. Sergeev, Phys. Rev. B **85**, 060501(R) (2012).
[16] A. W. Baggaley, L. K. Sherwin, C. F. Barenghi, and Y. A. Sergeev, Phys. Rev. B **86**, 104501 (2012).
[17] A. Cidrim, A. C. White, A. J. Allen, V. S. Bagnato, and C. F. Barenghi, Phys. Rev. A **96**, 023617 (2017).
[18] Á. V. M. Marino, L. Madeira, A. Cidrim, F. E. A. dos Santos, and V. S. Bagnato, Eur. Phys. J.: Spec. Top. **230**, 809 (2021).
[19] J. I. Polanco, N. P. Müller, and G. Krstulovic, Nat. Commun. **12**, 7090 (2021).
[20] A. L. Fetter, Laser Phys. **18**, 1 (2008).
[21] A. L. Fetter, Phys. Rev. A **64**, 063608 (2001).
[22] N. R. Cooper, S. Komineas, and N. Read, Phys. Rev. A **70**, 033604 (2004).
[23] V. K. Tkachenko, Solid State Phys. **22**, 1282 (1965).
[24] C. D. Andereck and W. I. Glaberson, J. Low Temp. Phys. **48**, 257 (1982).
[25] E. B. Sonin, Phys. Rev. A **72**, 021606(R) (2005).
[26] K. Hossain, K. Kobuszewski, M. M. Forbes, P. Magierski, K. Sekizawa, and G. Wlazłowski, Phys. Rev. A **105**, 013304 (2022).
[27] F. Waleffe, Phys. Fluids **5**, 677 (1993).
[28] C. Cambon, N. N. Mansour, and F. S. Godeferd, J. Fluid Mech. **337**, 303 (1997).
[29] C. Cambon, R. Rubinstein, and F. S. Godeferd, New J. Phys. **6**, 73 (2004).
[30] A. Pouquet and P. D. Mininni, Philos. Trans. R. Soc. A **368**, 1635 (2010).
[31] A. Sen, P. D. Mininni, D. Rosenberg, and A. Pouquet, Phys. Rev. E **86**, 036319 (2012).
[32] P. Clark Di Leoni, A. Alexakis, L. Biferale, and M. Buzzicotti, Phys. Rev. Fluids **5**, 104603 (2020).
[33] F. Bellet, F. S. Godeferd, J. F. Scott, and C. Cambon, J. Fluid Mech. **562**, 83 (2006).
[34] S. Galtier, Phys. Rev. E **68**, 015301(R) (2003).
[35] J. F. Scott, J. Fluid Mech. **741**, 316 (2014).
[36] A. Sedrakian and I. Wasserman, Phys. Rev. A **63**, 063605 (2001).
[37] C. J. Pethick and Smith, *Bose-Einstein Condensation in Dilute Gases* (Cambridge University Press, Cambridge, 2001).
[38] G. Baym, Phys. Rev. Lett. **91**, 110402 (2003).
[39] S. Kida and S. A. Orszag, J. Sci. Comput. **5**, 85 (1990).
[40] P. D. Mininni, D. Rosenberg, R. Reddy, and A. Pouquet, Parallel Comput. **37**, 316 (2011).
[41] M. Fontana, O. P. Bruno, P. D. Mininni, and P. Dmitruk, Comput. Phys. Commun. **256**, 107482 (2020).
[42] A. K. Verma, R. Pandit, and M. E. Brachet, Phys. Rev. Research **4**, 013026 (2022).

[43] V. Schweikhard, I. Coddington, P. Engels, V. P. Mogendorff, and E. A. Cornell, Phys. Rev. Lett. **92**, 040404 (2004).
[44] S. Stringari, Phys. Rev. Lett. **77**, 2360 (1996).
[45] G. Gauthier, M. T. Reeves, X. Yu, A. S. Bradley, M. A. Baker, T. A. Bell, H. Rubinsztein-Dunlop, M. J. Davis, and T. W. Neely, Science **364**, 1264 (2019).
[46] S. P. Johnstone, A. J. Groszek, P. T. Starkey, C. J. Billington, T. P. Simula, and K. Helmerson, Science **364**, 1267 (2019).
[47] F. Dalfovo, S. Giorgini, L. P. Pitaevskii, and S. Stringari, Rev. Mod. Phys. **71**, 463 (1999).
[48] C. F. Barenghi, Y. A. Sergeev, and A. W. Baggaley, Sci. Rep. **6**, 35701 (2016).
[49] C. F. Barenghi, V. S. L'vov, and P.-E. Roche, Proc. Natl. Acad. Sci. USA **111**, 4683 (2014).
[50] J. Clyne, P. Mininni, A. Norton, and M. Rast, New J. Phys. **9**, 301 (2007).
[51] D. Kivotides, J. C. Vassilicos, D. C. Samuels, and C. F. Barenghi, Phys. Rev. Lett. **86**, 3080 (2001).
[52] P. Clark di Leoni, P. D. Mininni, and M. E. Brachet, Phys. Rev. A **95**, 053636 (2017).
[53] T. P. Simula, P. Engels, I. Coddington, V. Schweikhard, E. A. Cornell, and R. J. Ballagh, Phys. Rev. Lett. **94**, 080404 (2005).
[54] L. Onsager, Nuovo Cimento **6**, 279 (1949).